IEEE Access
Multidisciplinary | Rapid Review | Open Access Journal

Received September 1, 2021, accepted September 5, 2021, date of publication September 7, 2021,
date of current version September 15, 2021.

Digital Object Identifier 10.1109/ACCESS.2021.3111015

Simultaneous Optimization of Virtual Synchronous Generators (VSG) Parameters in Islanded Microgrids Supplying Induction Motors

BAHRAM POURNAZARIAN[1], (Graduate Student Member, IEEE), REZA SANGRODY[2], MEYSAM SAEEDIAN[1], MATTI LEHTONEN[1], AND EDRIS POURESMAEIL[1], (Senior Member, IEEE)

[1]Department of Electrical Engineering and Automation, Aalto University, 02150 Espoo, Finland
[2]Department of Electrical and Computer Engineering, Firoozkooh Branch, Islamic Azad University, Firoozkooh 3981838381, Iran

Corresponding author: Edris Pouresmaeil (edris.pouresmaeil@aalto.fi)

ABSTRACT The growing importance of Microgrid in future power systems highlights critical challenges like microgrid control and stability. An islanded microgrid including distributed generations (DG), energy storage systems (ESS), and different types of loads (static or dynamic) is prone to instability. The whole microgrid system must be analyzed and designed to operate within stable regions. This study models an inverter-interfaced microgrid which supplies different types of loads such as static loads and symmetrical induction machines (SIM) by virtual synchronous generators (VSG). Afterwards, a generalized small-signal stability analysis framework is proposed for an islanded microgrid. This model is applied for stability analysis of an arbitrary islanded microgrid including several VSGs, lines, static loads, and SIM loads. Subsequently, permissible intervals for VSG parameters are drawn according to the microgrid small-signal stability analysis. These permissible intervals are compared for static and SIM load. Finally, a novel optimization platform is introduced which utilizes the particle swarm optimization (PSO) algorithm to draw optimal values for virtual impedances (VI), virtual inertia (Jv), virtual damping (D), and current state-feedback factor (F). The proposed optimization platform enhances the microgrid stability, minimizes voltage drops on the buses, the reactive power mismatches, and the frequency Nadir, simultaneously.

INDEX TERMS Current state-feedback factor (F), microgrid, symmetrical induction motors (SIM), small-signal stability, virtual synchronous generator (VSG), virtual impedance (VI).

I. INTRODUCTION

The revolution in electrical energy generation fosters the increasing penetration of renewable energy sources (RES) into traditional power systems. A microgrid as the bedrock for the RES integration, includes different DGs, ESS and loads which can be either islanded or connected to the main grid. The microgrid stability concept has been divided into two main categories, control system stability and power supply stability; A microgrid operating at an equilibrium point is stable if after being subjected to a small disturbance, all state variables reach novel final values which are inside the corresponding permissible intervals of microgrid [1]. A small-signal stability analysis could disclose stable intervals for controller parameters and droop coefficients by an eigenvalue analysis [2].

On the other hand, the virtual inertia concept has been introduced to enhance the microgrid stability by emulating the dynamic behavior of conventional synchronous generators and reducing the rate of change of frequency (ROCOF) and frequency Nadir [3]. Deploying Fuzzy controllers in VSG structure could facilitate damping transient perturbations by increasing the inertia of the system [4].

Applying a dual-adaptive inertia control method in a VSG could support the frequency characteristic better than the case with fixed virtual inertia [5]. The enhanced power decoupling

The associate editor coordinating the review of this manuscript and approving it for publication was Qiuye Sun.

mechanism in [6] applies virtual steady-state synchronous impedance and current compensation in the VSG controller to improve the dynamic performance and the stability of the system. The VSG parameters effects on performance indices have been analyzed in [7] and an algorithm has been proposed to tune these parameters to achieve the preferred performance indices.

However, the state-feedback damping method has been proposed to damp the low-frequency oscillations in grid-connected VSGs [8]. Similarly, the optimal distributed control in [9] has been proposed to enhance the microgrid small-signal stability and the dynamic performance of the secondary control mechanism in the microgrid. The small-signal modeling and parameter design of a single grid-connected VSG has been implemented in [10] to decrease the VSG voltage harmonics and decouple the active and reactive power loops. However, the optimization of VSG parameters in an islanded microgrid including induction motors, the reactive power sharing, and microgrid small-signal stability have not been analyzed in this reference.

Moreover, the internal model-based controllers (IMC) have shown a better performance than the proportional-integral (PI) controllers from the microgrid stability point of view [11]. The four-step optimization method in [12] has optimized the IMC-based controllers in an islanded microgrid and the proposed method has demonstrated an outstanding performance compared to the conventional droop control method.

The stable region of a DG has been estimated by Kernel Regression method which draws an analytical expression and facilitates the stable operation of an islanded microgrid [13]. The stability of a multi-machine power system could be enhanced using partial feedback linearizing excitation method which applies optimal control theory [14]. It has been reported that higher values of droop gains facilitate the faster power sharing but jeopardize the microgrid stability and a generalized power systems stabilizer (PSS) has been proposed in [15] to deal with this problem.

The small-signal stability of a microgrid including dynamic constant-power loads and drawing the permitted intervals for the microgrid parameters have been performed in [16], [17]. The detailed small-signal modeling and stability analysis of an islanded microgrid considering the dynamic behavior of phased-locked loop (PLL) device has been developed in [18].

The detailed modeling of a medium voltage microgrid including induction motor has been performed in [19] which has proposed an active damping controller to damp the oscillatory dynamics. The low-voltage ride through (LVRT) capability of a grid-connected medium-voltage microgrid including an induction machinery load has been enhanced in [20] and the microgrid small-signal stability has been analyzed. Another important high-power element is the isolated gate-driver power supply which has been designed in [21] for medium voltage applications and it has been compared in different insulation schemes.

However, virtual impedances as important elements in the microgrid power sharing adjustment affect the microgrid small-signal stability. The optimization of virtual inductances has been performed to remove the power coupling among several virtual synchronous generators [22]. Moreover, the feasible range of virtual impedances and their optimal values in a droop-controlled microgrid have been determined in [23]. The reactive power sharing and the microgrid stability index have been enhanced in [24] by employing optimal virtual impedances drawn by a PSO-based optimization method. On the other hand, the robust distributed control method proposed in [25] could share the active and reactive power among DGs using partial feedback linearization method.

The transient response of VSG has been improved through introducing dynamic droop gains and virtual impedances in [26] which has drawn the optimal controller gains by PSO optimization algorithm. The second harmonic current in dc-dc converters has been decreased in [27] by a novel control based on dc-bus port impedance. This method has limited the dc-link voltage ripple to mitigate second current harmonic in bus-voltage-controlled converter.

When several microgrid clusters are in interaction, the small-signal modeling and stability analysis of this system is a critical issue as reported in [28], which applies a novel distributed control method and optimizes the control parameters using PSO algorithm. A theoretical framework for the microgrid small-signal stability evaluation based on a distributed control methodology has been reported which considers the communication latency [29]. The stability condition of converter can change depending on the rectifying or inverting mode, absorbing or generating reactive power and the operating point as reported in [30]. Based on the previous literature review, the following research gaps are observed:

- The connection of directly-connected SIM jeopardize the microgrid small-signal stability. Permissible ranges of the VSG parameters must be defined considering these loads which has not been scrutinized in literature such as [11], [16], [18], [23], [24], [28].
- A range of stable parameters can be chosen for the VSG which result in different dynamic performance. The lack of a generalized optimization platform to optimize the VSG parameters and virtual impedances to efficiently and securely control and utilize the microgrid is seen.

The following contributions are achieved by this research:

- Permissible ranges of VSG parameters, virtual impedances, and current state-feedback factors are calculated in an islanded microgrid including a directly connected SIM.
- A novel small-signal stability framework is proposed for an islanded microgrid including arbitrary number of VSGs, lines, resistive-inductive loads, and SIMs.
- The simultaneous optimization of VSG parameters and virtual inertias in an islanded microgrid based on a novel methodology is devised and proposed. The microgrid small-signal stability, reactive power sharing, frequency Nadir and bus voltages are enhanced, simultaneously.

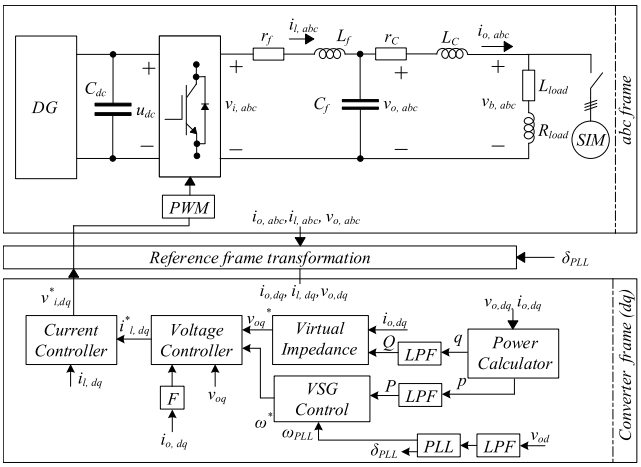

FIGURE 1. The proposed control block diagram of a typical VSG-based DG supplying a static load or a SIM.

The rest of this paper is organized as follows; The microgrid modeling and small-signal stability analysis are explained in section II. The proposed "VSG + VI + F" control method is introduced in section III. The simulation results are presented in section IV. Finally, section V terminates this study by drawing the conclusions. The Appendix and References are brought afterwards.

II. DYNAMIC MODELING OF MICROGRID

A virtual synchronous generator (VSG) supplying a load has a control block diagram as shown in Fig.1. The three-phase pre-filtering currents ($i_{l,abc}$), three-phase output currents ($i_{o,abc}$) and the three-phase output voltages ($v_{o,abc}$) are measured. A phased-lock loop (PLL) device is used to measure the actual frequency of positive components and the shift phase of the voltage. The control methodology is implemented on common dq reference frame [24].

A. SYMMETRICAL INDUCTION MOTOR (SIM) MODELING

The following dynamic equations describe the model in a dq reference-frame rotating at ω speed. The voltage components, v_{bD} and v_{bQ} are global bus voltage components (namely stator voltage components).

$$v_{bq} = r_s.i_{qs} + (\frac{X_{ss}}{\omega_b})\dot{i}_{qs} + (\frac{\omega}{\omega_b}X_{ss}).i_{ds} + (\frac{X_M}{\omega_b})\dot{i}'_{qr} + (\frac{\omega}{\omega_b}X_M).\dot{i}'_{dr} \quad (1)$$

$$v_{bd} = r_s.i_{ds} + (\frac{X_{ss}}{\omega_b})\dot{i}_{ds} - (\frac{\omega}{\omega_b}X_{ss}).i_{qs} + (\frac{X_M}{\omega_b}).\dot{i}'_{dr} - (\frac{\omega}{\omega_b}X_M).\dot{i}'_{qr} \quad (2)$$

where i_{qs} and i_{ds} are stator current components and $\dot{i}'_{qr}$ and $\dot{i}'_{dr}$ are derivative of rotor current components transmitted to the stator side.

Moreover, the dynamic equations (3) and (4) are written for rotor windings. $\omega, \omega_r, \omega_b$ are dq stator reference frame speed, rotor mechanical speed, and base angular speed for SIM, respectively [31]. v'_{qr} and v'_{dr} are rotor dq-voltages which are zero.

$$v'_{qr} = r'_r.i'_{qr} + (\frac{X_M}{\omega_b}).\dot{i}_{qs} + (\frac{\omega-\omega_r}{\omega_b}).X_M.i_{ds} + (\frac{X'_{rr}}{\omega_b}).\dot{i}'_{qr} + (\frac{\omega-\omega_r}{\omega_b}).X'_{rr}.i'_{dr} \quad (3)$$

$$v'_{dr} = r'_r.i'_{dr} + (\frac{X_M}{\omega_b}).\dot{i}_{ds} - (\frac{\omega-\omega_r}{\omega_b}).X_M.i_{qs} + (\frac{X'_{rr}}{\omega_b}).\dot{i}'_{dr} - (\frac{\omega-\omega_r}{\omega_b}).X'_{rr}.i'_{qr} \quad (4)$$

The state equation (5) calculates rotor angular velocity in terms of current components, electromagnetic torque (T_e) and load torque (T_L) [31].

$$\frac{d\omega_r}{dt} = (\frac{P}{2J})(T_e - T_L) = (\frac{P}{2J})\{\frac{3}{2}.\frac{P}{2}.L_M(i_{qs}.i'_{dr} - i_{ds}.i'_{qr}) - T_L\} \quad (5)$$

B. POWER CALCULATOR

Two instantaneous power components (p, q) are defined as functions of output voltages (v_{od}, v_{oq}) and currents (i_{od}, i_{oq}) of VSG units in (6) and (7). Two low-pass filters with the cut-off frequency of ω_c are applied in series with power calculator [18]. P and Q are the output active and reactive powers injected by the VSG to the microgrid.

$$p = \frac{3}{2}(v_{od}.i_{od} + v_{oq}.i_{oq}) \Rightarrow P = \frac{\omega_c}{s+\omega_c}.p \quad (6)$$

$$q = \frac{3}{2}(v_{oq}.i_{od} - v_{od}.i_{oq}) \Rightarrow Q = \frac{\omega_c}{s+\omega_c}.q \quad (7)$$

C. VIRTUAL IMPEDANCES

The virtual impedances block in Fig.1 assigns dq voltage references of the VSG according to (8). The control keeps d-axis voltage at zero by aligning the output voltage reference with the q-axis, therefore just the q-axis voltage set-point is dictated to the voltage controller. In this equation, first part is related to droop control ($n_q.Q$) and the second part is a term related to the virtual impedances [23].

$$v^*_{oq} = V_{oq_N} - n_q.Q - (R_v.i_{oq} + X_v.i_{od})$$
$$v^*_{od} = 0 \quad (8)$$

where V_{oq_N}, R_v, X_v and n_q are nominal q-axis voltage, virtual resistance, virtual reactance, and reactive power droop coefficient, respectively.

D. VSG CONTROLLER

The VSG block in the VSG control diagram is supposed to assign the frequency reference in dq reference frame [5]. The frequency reference (ω^*) is calculated according to instantaneous frequency (ω_{PLL}), nominal frequency (ω_n), active power (P) and virtual inertia (J_v) and virtual damping (D). Virtual synchronous generator (VSG) mimics the performance of inertia and damping of rotor in conventional

synchronous generators and P_0 is the nominal active power of VSG [5].

$$\dot{\omega}^* = -(D/J_v).(\omega^* - \omega_n) + (P_0 - P).1/(J_v\omega_n) - (\omega_{PLL} - \omega_n).(K_f/J_v) \quad (9)$$

E. VOLTAGE CONTROLLER

Equations (10) and (11) assign dq-current components in terms of terminal currents (i_{ld}, i_{lq}), current state-feedback factor (F), and auxiliary variables (ϕ_d and ϕ_q). ω_{PLL} is the angular frequency measured by PLL and ω^* is the angular frequency reference which is assigned by VSG controller block. The measured and reference value of q-axis voltage are compared in (11). Two PI controllers are applied in d and q axis directions and corresponding proportional and integral coefficients are k_{pv} and k_{iv}, respectively [3].

$$\dot{\phi}_d = \omega_{PLL} - \omega^* \Rightarrow i^*_{ld} = k_{iv}.\phi_d + k_{pv}.\dot{\phi}_d + F.i_{od} \quad (10)$$

$$\dot{\phi}_q = v^*_{oq} - v_{oq} \Rightarrow i^*_{lq} = k_{iv}.\phi_q + k_{pv}.\dot{\phi}_q + F.i_{oq} \quad (11)$$

The PLL model used in this study was proposed in [18]. Equations (12)-(14) explain the dynamic modeling of the PLL. ω_n and $\omega_{c,PLL}$ are the nominal frequency of the microgrid (rad/s) and cut-off frequency of the low-pass filter in PLL model, respectively [18].

$$\omega_{PLL} = \omega_n - k_{p,PLL}.v_{od,f} + k_{i,PLL}.\varphi_{PLL} \quad (12)$$

$$\dot{\varphi}_{PLL} = -v_{od,f} \quad (13)$$

$$\dot{v}_{od,f} = \omega_{c,PLL}.v_{od} - \omega_{c,PLL}.v_{od,f} \quad (14)$$

F. CURRENT CONTROLLER

Equations (15) and (16) determine the voltage commands in dq reference-frame in terms of terminal current components (i_{ld}, i_{lq}) and auxiliary variables (γ_d, γ_q). It should be noted that the ancillary state variables (γ_d, γ_q) facilitate the system formulation and physical equivalents for them are not found. Moreover, two PI controllers are applied in two directions (d, q) and the corresponding proportional and integral coefficients are k_{pc} and k_{ic} respectively [3].

$$\dot{\gamma}_d = i^*_{ld} - i_{ld} \Rightarrow v^*_{id} = -\omega_n.L_f.i_{lq} + k_{ic}.\gamma_d + k_{pc}.\dot{\gamma}_d \quad (15)$$

$$\dot{\gamma}_q = i^*_{lq} - i_{lq} \Rightarrow v^*_{iq} = \omega_n.L_f.i_{ld} + k_{ic}.\gamma_q + k_{pc}.\dot{\gamma}_q \quad (16)$$

III. SMALL-SIGNAL STABILITY ANALYSIS

A typical islanded microgrid including VSGs, lines, resistive-inductive loads (RL), and SIM loads is a non-linear dynamic system. A general microgrid model is shown in Fig.2 which facilitates the explanation of small-signal stability analysis. The state variables for any VSG, line, RL load, and SIM load are written in (17)–(21), respectively. The idea is to develop state matrix of microgrid (A_{MG}) and draw the microgrid eigenvalues by this matrix. The small-signal stability of microgrid is examined by the location and the damping ratio of dominant eigenvalues.

It is assumed in Fig.2 that a line connects buses k and i ($R_{line,ki} + \mathrm{j}.X_{line,ki}$) and buses i and j are connected by another line ($R_{line,ij} + \mathrm{j}.X_{line,ij}$). The state variables of VSGs i and j are listed in (17) and (18), respectively.

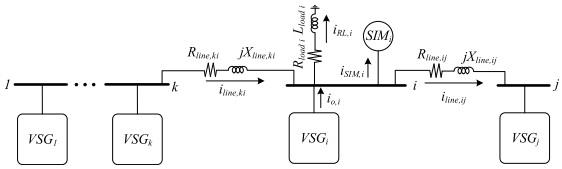

FIGURE 2. Typical microgrid under small-signal stability analysis.

$$x_{VSG,i} = [\delta_i, P_i, Q_i, \phi_{d,i}, \phi_{q,i}, \gamma_{d,i}, \gamma_{q,i}, i_{ld,i}, i_{lq,i}, \varphi_{PLL,i}, v_{odf,i}, \omega^*_i, v_{od,i}, v_{oq,i}, i_{od,i}, i_{oq,i}]^T_{1\times 16} \quad (17)$$

$$x_{VSG,j} = [\delta_j, P_j, Q_j, \phi_{d,j}, \phi_{q,j}, \gamma_{d,j}, \gamma_{q,j}, i_{ld,j}, i_{lq,j}, \varphi_{PLL,j}, v_{odf,j}, \omega^*_j, v_{od,j}, v_{oq,j}, i_{od,j}, i_{oq,j}]^T_{1\times 16} \quad (18)$$

$$x_{Line,i} = [i_{lineD,i}, i_{lineQ,i}]^T_{1\times 2} \quad (19)$$

$$x_{RL,i} = [i_{loadD,i}, i_{loadQ,i}]^T_{1\times 2} \quad (20)$$

$$x_{SIM,i} = [i_{Qs,i}, i_{Ds,i}, i'_{Qr,i}, i'_{Dr,i}, \omega_{r,i}]^T_{1\times 5} \quad (21)$$

The dq reference frame of VSG1 is considered as the common reference frame. The state variables of this VSG are seen in (22).

$$x_{VSG,com} = [\delta_{PLL,1}, P_1, Q_1, \phi_{d,1}, \phi_{q,1}, \gamma_{d,1}, \gamma_{q,1}, i_{ld,1}, i_{lq,1}, \varphi_{PLL,1}, v_{odf,1}, \omega^*_i, v_{od,1}, v_{oq,1}, i_{od,1}, i_{oq,1}]^T_{1\times 16} \quad (22)$$

The differential change of state variables of $line_{ij}$, $line_{ki}$, RL_i, and SIM_i are written in (23)–(26), respectively. The loads and lines state variables are expressed in common (DQ) reference frame.

$$\Delta x_{line,ij} = [\Delta i_{lineD,ij}, \Delta i_{lineQ,ij}]^T \quad (23)$$

$$\Delta x_{line,ki} = [\Delta i_{lineD,ki}, \Delta i_{lineQ,ki}]^T \quad (24)$$

$$\Delta x_{RL,i} = [\Delta i_{loadD,i}, \Delta i_{loadQ,i}]^T \quad (25)$$

$$\Delta x_{SIM,i} = [\Delta i_{Qs,i}, \Delta i_{Ds,i}, \Delta i'_{Qr,i}, \Delta i'_{Dr,i}, \Delta\omega_{r,i}]^T_{1\times 5} \quad (26)$$

The typical bus i in a general islanded MG (Fig.2) consisting of p VSGs, q lines, r RL loads, and s SIM loads is considered. The state space equations of VSG_i are drawn and linearized around an operating point. These equations are seen as (27) and (28).

$$\begin{aligned}&[\Delta\dot{\delta}_{PLL,i}\ \Delta\dot{P}_i\ \Delta\dot{Q}_i\ \Delta\dot{\phi}_{d,i}\ \Delta\dot{\phi}_{q,i}\ \Delta\dot{\gamma}_{d,i}\\ &\quad \Delta\dot{\gamma}_{q,i}\ \Delta\dot{i}_{ld,i}\ \Delta\dot{i}_{lq,i}\ \Delta\dot{\varphi}_{PLL,i}\ \Delta\dot{v}_{odf,i}\ \Delta\dot{\omega}^*_i]^T\\ &= A_1.\Delta x_{VSG,i} + A_2.\Delta x_{VSG,com}\end{aligned} \quad (27)$$

$$\begin{aligned}&[\Delta\dot{v}_{od,i}\ \Delta\dot{v}_{oq,i}\ \Delta\dot{i}_{od,i}\ \Delta\dot{i}_{oq,i}]^T = A_3.\Delta x_{VSG,i}\\ &\quad + A_4.\Delta x_{VSG,com} + A_5.\Delta x_{RL,i} + A_6.\Delta x_{SIM,i}\\ &\quad + A_7.\Delta x_{line,ij} - A_7.\Delta x_{line,ki}\end{aligned} \quad (28)$$

where A_1–A_{21} matrices are explained in Appendix B. The small-signal equations for a transmission line between buses i and j is expressed by (29).

$$\begin{aligned}\Delta\dot{x}_{line,ij} &= A_8.\Delta x_{VSG,i} + A_9.\Delta x_{VSG,j}\\ &\quad + A_{10}.\Delta x_{RL,i} - A_{10}.\Delta x_{RL,j} + A_{11}.\Delta x_{SIM,i}\\ &\quad - A_{11}.\Delta x_{SIM,j} + A_{12}.\Delta x_{line,ij} - A_{12}.\Delta x_{line,ki}\end{aligned} \quad (29)$$

The small-signal equations for a RL load installed at bus i are explained in (30).

$$\begin{aligned}\Delta\dot{x}_{RL,i} = {} & A_{13}.\Delta x_{VSG,i} + A_{14}.\Delta x_{VSG,com} \\ & + A_{15}.\Delta x_{RL,i} + A_{16}.\Delta x_{SIM,i} \\ & + A_{17}.\Delta x_{line,ij} - A_{17}.\Delta x_{line,ki}\end{aligned} \tag{30}$$

The small-signal equations for a SIM load installed at bus i are illustrated in (31).

$$\begin{aligned}\Delta\dot{x}_{SIM,i} = {} & E^{-1}.\{(F + A_{18}).\Delta x_{SIM,i} + A_{19}.\Delta x_{VSG,i} \\ & + A_{20}.\Delta x_{RL,i} + A_{21}.\Delta x_{line,ij} - A_{21}.\Delta x_{line,ki}\}\end{aligned} \tag{31}$$

where A_1-A_{21}, E, and F matrices are explained in Appendix. The equations (27)–(31) present the small-signal equations for all VSGs, lines, RL loads, and SIM loads in terms of individual local state variables. Since a microgrid consists of several VSGs, lines, and loads, the next step is to assume the microgrid as a system and rewrite the state equations in terms of microgrid state variables.

$$\begin{aligned}x_{MG} = {} & [x_{VSG,1}, \ldots, x_{VSG,p}, x_{line,1}, \ldots, x_{line,q}, \\ & x_{RL,1}, \ldots, x_{RL,r}, x_{SIM,1}, \ldots, x_{SIM,s}]^T_{1\times(16p+2q+2r+5s)}\end{aligned} \tag{32}$$

The state-equations (27)–(31) can be straightforwardly written in terms of microgrid state matrix (32). The zero rows and columns are added to any of A_i matrices in (27)–(31) for the entries which do not have non-zero values to form matrices with $16p+2q+2r+5s$ columns. For the simplicity in notation, it is assumed that $N = 16p + 2q + 2r + 5s$. For example, in a 3 bus microgrid including three VSGs, two lines, one RL load, and one SIM load, there are $N = 55$ state variables.

Since the state equations for VSG_i are expressed by (27) and (28), to present these equations in terms of MG variables, all A_i matrices are rewritten in a suitable way so as they will finally have N columns. For instance, the matrix A'_1 while applying (28) for VSG 1 is written so as the A_1 is located in columns 1–16 of A'_1 and the other entries of A'_1 are zero.

$$A'_{1,VSG1} = \left[\underbrace{[A_1]_{12\times16}}\quad\overbrace{\cdots}^{\text{zero columns}}\right]_{12\times N} \tag{33}$$

However, the matrix A'_1 while applying (28) for VSG 2 is written as (34).

$$A'_{1,VSG2} = \left[\overbrace{\cdots}^{\text{16 zero columns}}\quad\underbrace{[A_1]_{12\times16}}\quad\overbrace{\cdots}^{\text{zero columns}}\right]_{12\times N} \tag{34}$$

The indices VSG1, VSG2, etc in (33), (34), etc are removed hereafter to simplify the notation of matrices. The same argument holds for A'_2–A'_{21} matrices. By substituting the corresponding matrices in (27) it is concluded that:

$$\begin{aligned}&[\Delta\dot{\delta}_{PLL,i}\ \ \Delta\dot{P}_i\ \ \Delta\dot{Q}_i\ \ \Delta\dot{\phi}_{d,i}\ \ \Delta\dot{\phi}_{q,i}\ \ \Delta\dot{\gamma}_{d,i} \\ &\quad \Delta\dot{\gamma}_{q,i}\ \ \Delta\dot{i}_{ld,i}\ \ \Delta\dot{i}_{lq,i}\ \ \Delta\dot{\varphi}_{PLL,i}\ \ \Delta\dot{v}_{odf,i}\ \ \Delta\dot{\omega}^*_i]^T \\ &= (A'_1 + A'_2).\Delta x_{MG}\end{aligned} \tag{35}$$

The equation (28) is rewritten in the same way applying $A'_3,\ldots,A'_7$ as follows.

$$\begin{aligned}[\Delta\dot{v}_{od,i}\ \ \Delta\dot{v}_{oq,i}\ \ \Delta\dot{i}_{od,i}\ \ \Delta\dot{i}_{oq,i}]^T = {} & (A'_3 + A'_4 + A'_5 \\ & + A'_6 + A'_7 - A''_7).\Delta x_{MG}\end{aligned} \tag{36}$$

where A'_3–A'_7 are calculated by the inserting zero rows and columns in a suitable way, as it was explained previously. The matrix A''_7 is obtained by using A_7 and the only difference with A'_7 is the locations of their non-zero columns and rows. The small-signal deviation of VSG state in terms of microgrid state is calculated by (37).

$$\Delta\dot{x}_{VSG,i} = \underbrace{\begin{bmatrix}[A'_1 + A'_2]_{12\times N} \\ [A'_3 + A'_4 + A'_5 + A'_6 + A'_7 - A''_7]_{4\times N}\end{bmatrix}}_{A_{VSG,i}}\Delta x_{MG} \tag{37}$$

The same routine is followed to write the equations (29)–(31) in terms of microgrid state variables. The small-signal equations of a line between buses i and j in terms of microgrid state are written in (38). Moreover, the differential change of the state of an RL load installed in bus i is calculated by (39).

$$\begin{aligned}\Delta\dot{x}_{line,ij} = {} & (A'_8 + A'_9 + A'_{10} - A''_{10} \\ & + \underbrace{A'_{11} - A''_{11} + A'_{12} - A''_{12}}_{A_{line,i}}).\Delta x_{MG}\end{aligned} \tag{38}$$

$$\Delta\dot{x}_{RL,i} = \underbrace{(A'_{13} + A'_{14} + A'_{15} + A'_{16} + A'_{17} - A''_{17})}_{A_{RL,i}}.\Delta x_{MG} \tag{39}$$

In order to express (31) in terms of microgrid state variables, the following matrices are defined.

$$\begin{aligned}B_1 &= E^{-1}(F + A_{18}) \\ B_2 &= E^{-1}(A_{19}) \\ B_3 &= E^{-1}(A_{20}) \\ B_4 &= E^{-1}(A_{21})\end{aligned} \tag{40}$$

The matrices B'_1-B'_4 are calculated by following the similar method like $A'_1,\ldots,A'_4$. The equation (31) is rewritten using the matrices in (40) in terms of microgrid state variables.

$$\Delta\dot{x}_{SIM,i} = \underbrace{(B'_1 + B'_2 + B'_3 + B'_4 - B''_4)}_{A_{SIM,i}}.\Delta x_{MG} \tag{41}$$

After drawing all state equations of VSGs, lines, RL loads, and SIM loads in terms of microgrid state variables (x_{MG}), the state space representation of MG including p VSGs, q lines and r RL loads, and s SIM loads is written as by (42).

$$\Delta\dot{x}_{MG} = A_{MG}.\Delta x_{MG} \tag{42}$$

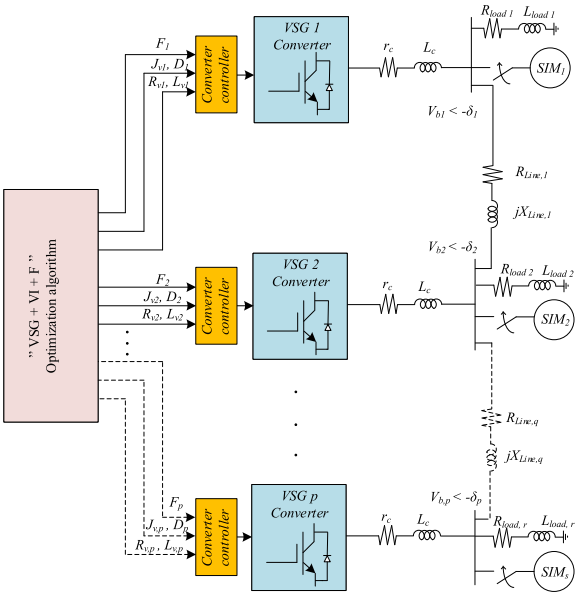

FIGURE 3. The application of "VSG + VI + F" optimization algorithm to control an island microgrid.

$$A_{MG} = \begin{bmatrix} [A_{VSG1}]_{16\times N} \\ \vdots \\ [A_{VSG,p}]_{16\times N} \\ [A_{line,1}]_{2\times N} \\ \vdots \\ [A_{line,q}]_{2\times N} \\ \vdots \\ [A_{RL,1}]_{2\times N} \\ \vdots \\ [A_{RL,r}]_{2\times N} \\ \vdots \\ [A_{SIM,1}]_{5\times N} \\ \vdots \\ [A_{SIM,s}]_{5\times N} \end{bmatrix}_{N\times N} \tag{43}$$

The *eig* command in MATLAB is applied to draw the eigenvalues of the MG as follows.

$$\text{Microgrid eigenvalues} = eig(A_{MG}) \tag{44}$$

The microgrid is asymptotically stable if it has one eigenvalue located at zero and all other eigenvalues have negative real parts.

IV. THE PROPOSED "VSG + VI + F" OPTIMIZATION ALGORITHM

The application of the proposed "VSG + VI + F" algorithm is demonstrated in Fig.3 which is meant to draw optimal values for J_v, D, R_v, L_v, and F. In this microgrid, there are a range of virtual inertia (J_v), virtual damping (D), virtual impedances (R_v, L_v), and current state-feedback (F) for each of VSG which guarantees the stable operation of microgrid.

The damping ratio of an eigenvalue is defined in terms of its real and imaginary parts as seen in (45).

$$\zeta(Z = Re + j.Im) = \frac{|\ Re\ |}{\sqrt{(Re^2 + Im^2)}} \tag{45}$$

The minimum damping ratio at operating point i which has e eigenvalues is defined by (46) as

$$\begin{aligned} \zeta^i_{min} &= \text{minimum}\{\zeta_1, \zeta_2, \ldots, \zeta_e\} \text{ at operating point } i \\ \text{e} &= \text{number of microgrid eigenvalues} \end{aligned} \tag{46}$$

If the study horizon include m operating points, the minimum damping ratio of microgrid is defined as

$$\begin{aligned} \zeta_{min} &= \text{minimum}\{\zeta^1_{min}, \zeta^2_{min}, \ldots, \zeta^m_{min}\} \\ \text{m} &= \text{number of operating points} \end{aligned} \tag{47}$$

Using the previous equations, the microgrid stability index is defined in (48). It should be noted that, minimizing SI leads to a better damping ratio for the critical eigenvalue.

$$SI = 1 - \zeta_{min} \quad (0 < \zeta_{min} \leq 1) \tag{48}$$

Equation (49) aims at measuring the reactive power mismatches which is used then in the objective function. The reactive power droop coefficient of VSG_j and $VSG_{(j+1)}$ are notated by $n_{q,j}$ and $n_{q,j+1}$, respectively to calculate the effective share of any VSG from the total reactive power mismatch.

$$\begin{aligned} \Delta Q &= \sum_{j=1}^{n_{DG}-1} max\ |\ \frac{n_{q,j}.Q_j - n_{q,j+1}.Q_{j+1}}{Q_0}\ | \\ &= max\ |\ \frac{X(:,3) - X(:,19)}{Q_0}\ | \\ &\quad + max\ |\ \frac{X(:,19) - X(:,35)}{Q_0}\ | \end{aligned} \tag{49}$$

where Q_0 is the base power to make the values per-unit and X is the state vector of microgrid and its dimension is $num \times 59$ and num is obtained by dividing the simulation time duration to the simulation time-step. $X(:,3)$, $X(:,19)$ and $X(:,35)$ are reactive powers injected by VSGs 1, 2 and 3 in all operating points, respectively. The frequency Nadir is calculated by (50) and is a function of virtual damping (D) of VSG [32].

$$\begin{aligned} &\Delta\omega_{max} \\ &= |\ \frac{\omega_{min} - \omega_n}{\omega_n}\ | \\ &= |\ \frac{min(\omega_n - k_{p,PLL}.X(:,11) + k_{i,PLL}.X(:,10)) - \omega_n}{\omega_n}\ | \end{aligned} \tag{50}$$

where $X(:,10)$, $X(:,11)$ are φ_{PLL1}, v_{odf1} in all operating points, respectively. ω_n is the nominal frequency of VSG (rad/s). Considering these major concerns, the proposed objective function is written as seen in (51).

$$O.F. = p_1.SI + p_2.\Delta Q + p_3.\Delta\omega_{max} \tag{51}$$

where the terms $0 < p_1, p_2, p_3 < 1$ are weighting coefficients which are assigned based on the priorities of the microgrid.

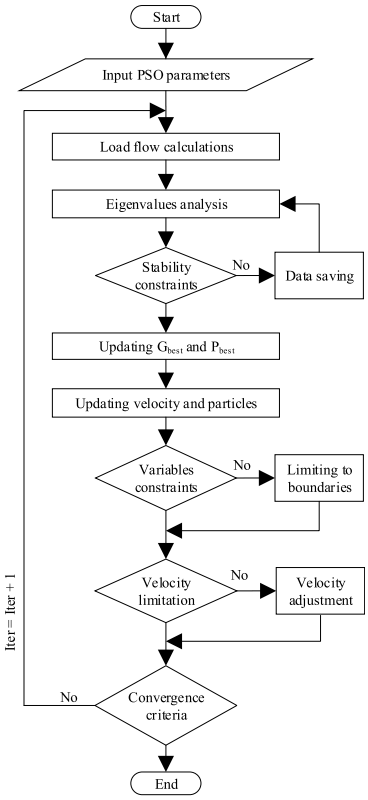

FIGURE 4. The proposed "VSG + VI + F" optimization algorithm.

The weighting factors are chosen between 0 and 1 and the summation of them is equal to 1. It should be noted that the converters voltage drops are controlled by limiting the permissible ranges of virtual resistances and virtual inductances.

The proposed "VSG + VI + F" optimization algorithm is demonstrated in Fig.4 and its operational steps are explained as follows.

- *Start:*
  An initial population for PSO algorithm is made based on initial values of optimization variables:

$$y_0 = [J_{v1}, D_1, F_1, R_{v1}, L_{v1}, J_{v2}, D_2, F_2 \\ R_{v2}, L_{v2}, J_{v3}, D_3, F_3, R_{v3}, L_{v3}] \quad (52)$$

- *Input PSO Parameters:*
  The PSO algorithm parameters are entered as seen in Table 1.
- *Load Flow Calculations:*
  The microgrid load flow in MATLAB is run to draw different operating points (m points).
- *Eigenvalues Analysis:*
  The eigenvalues of the microgrid at operating point x_i are calculated. The minimum value of ζ^i_{min} among m operating points and e eigenvalues is chosen as the critical point and its damping ratio is ζ_{min}. The microgrid stability index is $1 - \zeta_{min}$.
- *Stability Constraints:*
  Then, if any of operating points is unstable for this solution, an infinite value is attributed to SI so as this solution is ignored by PSO.
- *Data Saving:*
  The stable operating points with corresponding values of microgrid stability index, reactive power mismatches, frequency nadir, and their corresponding value of objective function are saved.
- *Updating G_{best} and $P_{i,best}$:*
  The values of personal experience ($P_{i,best}$) and global experience (G_{best}) are the lowest values of cost function experienced by any particle in its transitions and experienced by the whole population, respectively.
- *Updating Velocities and Particles:*
  The velocity of i^{th} particle ($V_i^{(k)}$) is updated in terms of its current location ($y_i^{(k)}$), its best personal experience ($P_{i,best}$), and the best experience of the whole population (G_{best}) [33].

$$V_i^{(k)} = \omega.V_i^{(k)} + r_1.c_1(P_{i,best} - y_i^{(k)}) \\ + r_2.c_2(G_{best} - y_i^{(k)}) \quad (53)$$

  where ω, c_1, and c_2 are inertia weight, personal learning coefficient and global learning coefficient, respectively. The coefficients r_1 and r_2 are obtained by uniform random distribution in the interval of (0,1) by *rand* function in MATLAB. The location of any particle ($y_i^{(k)}$) in k^{th} movement is updated by (54).

$$y_i^{(k)} = y_i^{(k)} + V_i^{(k)} \quad (54)$$

- *Variables Constraints:* A minimum and maximum for any optimization variable ($J_v, D, F, \ldots$) is considered based on the microgrid stability analysis and permissible voltage drop. These values are placed in two different matrices ($[VarMin]_{1\times 9}$, $[VarMax]_{1\times 9}$) to facilitate the simulation in MATLAB.
- *Limiting to Boundaries:* If the value of any variable is outside of its permissible interval, its value is forced to the boundary value.
- *Velocity Limitation:* The velocity of particles are limited to stay inside the optimization domain as explained by (55).

$$V_{i,max} = \alpha.(y_{i,max} - y_{i,min}) \\ V_{i,min} = -\alpha.(y_{i,max} - y_{i,min}) \quad (55)$$

- *Velocity Adjustment:* If the velocity of particles are forced to stay in permitted intervals as seen in (56).

$$V_i^{(k)} = min\{max\{V_i^{(k)}, V_{i,min}\}, V_{i,max}\} \quad (56)$$

- *Convergence Criteria:* If the algorithm is converged, the optimal solution is exported, otherwise the next iteration is begun.
- *End:* A set of optimized values (F, J_v, D, R_v, L_v) are exported.

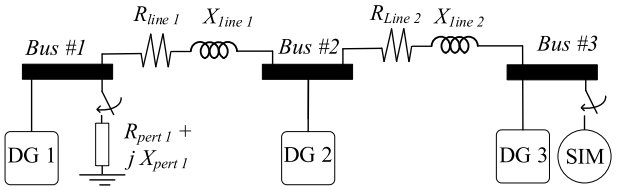

FIGURE 5. Three bus test microgrid.

TABLE 1. PSO algorithm parameters.

Parameter	Value	Parameter	Value
$Iter, w$	100, 0.7298	$nPop, nVar$	10, 9
c_1, c_2	1.4962, 1.4962	α	0.1
F_{min}, D_{min}	0, 91.2	F_{max}, D_{max}	0.74, 300
$J_{v,min}$	0.01 $kg.m^2$	$J_{v,max}$	11 $kg.m^2$
$R_{v1,min}, L_{v1,min}$	0 Ω, 0 H	$R_{v1,max}, L_{v1,max}$	0.2 Ω, 0.01H
$R_{v2,min}, L_{v2,min}$	0 Ω, 0 H	$R_{v2,max}, L_{v2,max}$	0.2 Ω, 0.01 H
$R_{v3,min}, L_{v3,min}$	0 Ω, 0 H	$R_{v3,max}, L_{v3,max}$	0.2 Ω, 0.01 H

TABLE 2. SIM parameters.

Parameter	Value	Parameter	Value
P, V	3 hp, 380 V	T_B, ω_b	11.9 $N.m$, 1710 rpm
X_{ls}, r_s	50.26 Ω, 0.435 Ω	J, X'_{lr}	0.089 $kg.m^2$, 0.754 Ω
r'_r	0.816 Ω	X_M	26.13 Ω

TABLE 3. VSGs parameters.

Parameter	Value	Parameter	Value
L_f, C_f	1.35 mH, 50 μF	r_f, r_n	0.1 Ω, 1000 Ω
r_c, ω_c	0.03 Ω, 31 rad/s	L_c, ω_n	0.35 mH, 314 rad/s
$\omega_{c,PLL}$	7853.98 rad/s	n_q	0.0013 V/Var
V_{oqN}	380 V	K_f	0.1
R_{load1}	25 Ω	R_{line1}	0.23 Ω
L_{load1}	15 mH	X_{line1}	0.1 Ω
R_{line2}	0.35 Ω	R_{pert1}	25 Ω
X_{line2}	0.58 Ω	L_{pert1}	0.1 mH
$k_{p,PLL}, P_0$	0.25, 10 kW	k_{pv}	1
$k_{i,PLL}, k_{iv}$	2, 250	k_{pc}, k_{ic}	10, 1600

V. SIMULATION RESULTS

The test microgrid depicted in Fig.5 which includes a SIM load and a RL load is simulated in this study. The PSO algorithm parameters, SIM parameters, and VSGs parameters are listed in Table 1, Table 2 and Table 3, respectively. The load change scenario occurs at t = 2 s when a 5.8 kW static load ($R_{pert1} + j\omega_n.L_{pert1}$) is switched in at bus 1 in parallel with its initial load of $R_{load1}+j.X_{load1}$. The bus 2 is in no-load condition. The initial load of bus 3 is also zero and the load torque of 5 × 11.9 N.M is enforced to the motor in bus 3 at t = 4 s.

A. PERMISSIBLE RANGES OF PARAMETERS

The small-signal stability analysis for the 3-bus microgrid demonstrated in Fig.5 is performed and the permissible intervals for control parameters are drawn. The permissible ranges of parameters in two cases are compared; firstly to have a 5.8 kW (25 Ω per phase) static load at bus 3 of microgrid and secondly to have the SIM (described in Table 2) at bus 3. In both cases the load at bus 1 is 5.8 kW and bus 2 has no local load.

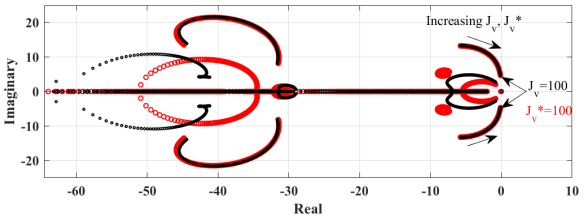

FIGURE 6. The microgrid eigenvalues while changing virtual inertia (J_v) in presence of static load (black curve) or SIM load (red curve).

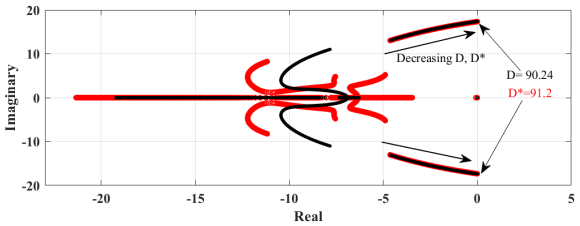

FIGURE 7. The microgrid eigenvalues while changing virtual damping (D) in presence of static load (black curve) or SIM load (red curve).

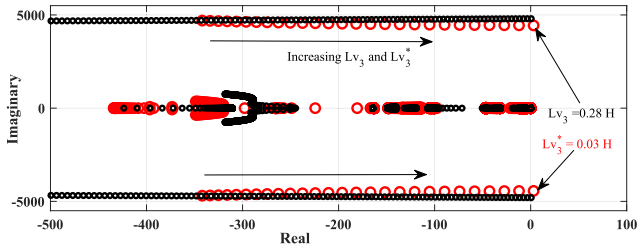

FIGURE 8. The microgrid eigenvalues while changing virtual inductance of VSG 3 in presence of static load (black curve) or SIM load (red curve).

The first major parameter is the virtual inertia (J_v) which significantly changes the dynamic performance of the VSG. Fig.6 demonstrates the major eigenvalues of the microgrid while changing virtual inertia (J_v) from 0.001 to 100 $kg.m^2$ in two cases. It is seen that the permissible ranges of J_v either by having a static load or a SIM at bus 3 are identical.

The virtual damping which affects the steady-state frequency Nadir is changed in Fig.7. The minimum permissible value for D are 90.8 and 91.2 for static load and SIM load, respectively. The upper bound is ∞ which means the greater values would not make the microgrid unstable.

The major eigenvalues of microgrid while changing the virtual inductance of VSG 3 are shown in Fig.8. The maximum permissible value of virtual inductance of VSG 3 while supplying a static load or a SIM at bus 3 are 0.28 H and 0.03 H respectively. Installing a SIM apparently decreases the permissible range of virtual inductance in the corresponding bus. As the effect on the permissible ranges of the other buses are minor, they have not been demonstrated here. The virtual resistance of VSG 3 is changed from 0 to ∞ and the major eigenvalues of microgrid are depicted in Fig.9. It is seen that the maximum permissible value of virtual resistor at VSG 3 is 10.68 Ω while having a static load at bus 3, but the maximum

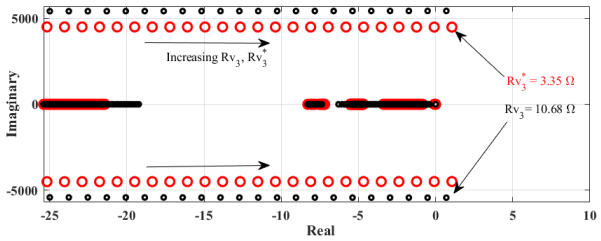

FIGURE 9. The microgrid eigenvalues while changing virtual resistance of VSG 3 in presence of static load (black curve) or SIM load (red curve).

TABLE 4. Optimal controller parameters.

Proposed optimal parameters		Method in [24]	
F, J_v	0.337, 5.66	F, J_v	0.132, 6.37
D, L_{v1}	294.80, 0.0046	D, L_{v1}	213.71, 0.007
L_{v2}, L_{v3}	0.0035, 0.0074	L_{v2}, L_{v3}	0.00598, 0.00715
R_{v1}, R_{v2}	0.0707, 0.14371	R_{v1}, R_{v2}	0.10065, 0.05793
R_{v3}	0.12455	R_{v3}	0.16430
p_1, p_2	0.2, 0.6	p_3	0.2

permissible virtual resistance while having the SIM load at bus 3 is 3.35 Ω which is roughly one third of the former value while having static load at bus 3.

B. DYNAMIC PERFORMANCE OF VSGs

The optimal parameters drawn by the proposed "VSG + VI + F" optimization algorithm and the objective function in [24] are listed in Table 4. Hereafter, different dynamic characteristics of the 3-bus microgrid are analyzed.

1) VOLTAGE COMPONENTS OF VSGs

It is seen in Fig.10a that both methods show a similar steady state d-axis voltage which is forced to be zero in both control methods. The maximum d-axis voltage deviations are -1 V, -1.4, by the proposed method and one in [24], respectively. However, the q-axis voltage while applying the proposed control method reaches at 367.30 V at t = 5 s in bus 3, while the results drawn from [24] demonstrate the lowest voltage of 365.56 V in bus 3. Consequently, applying the optimal parameters obtained from the proposed optimization algorithm enhanced the voltage by 1.74 V.

2) FREQUENCY OF THE MICROGRID

It is seen in Fig.11 that the frequency Nadir using the proposed control method is lower than the corresponding frequency while applying the optimal control parameters drawn from [24]. The frequency Nadir is enhanced from 49.92 Hz to 49.94 Hz by applying the proposed optimal control parameters in this study. It should be noted the change in frequency Nadir can be controlled by the corresponding weighting coefficient in the objective function.

3) MAJOR EIGENVALUES OF THE MICROGRID

The dominant eigenvalues of the 3-bus test microgrid are demonstrated in Fig.12. The critical eigenvalues (A) have

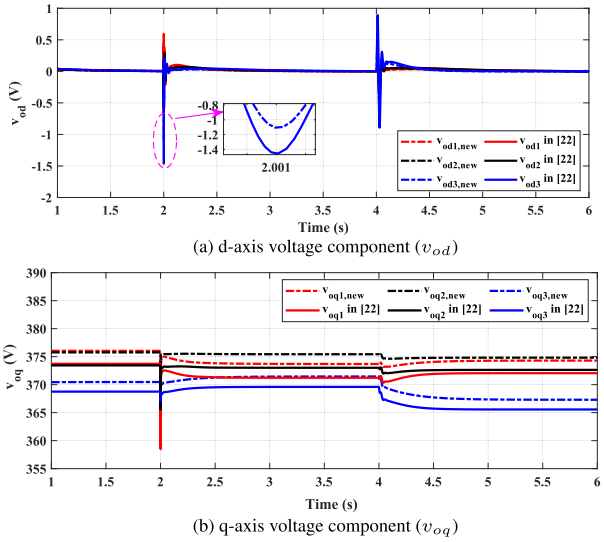

FIGURE 10. The microgrid voltage components for VSGs 1, 2, 3 in load change scenario applying the proposed optimal parameters and the optimal parameters in [24].

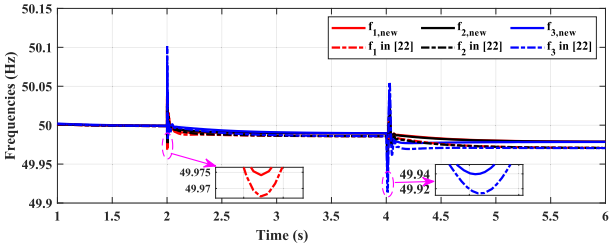

FIGURE 11. The microgrid frequency in load change scenario for VSGs 1,2, and 3 while applying the proposed optimal parameters and the optimal parameters in [24].

been -2.92 ± 17.12 and -0.36 ± 20.7 while using the proposed optimization method and the optimization method in [24], respectively. The corresponding damping ratios of this eigenvalues have been 16.81 % and 1.7 %, respectively. Therefore, the proposed optimization method prominently enhanced the microgrid small-signal compared to the method in [24]. The minimum damping ratio at point B using the proposed method has been 78.05 % and the minimum value by the method in [24] is 74.33 % and these modes are also better damped using the proposed control method. The other non-dominant modes have a negligible effect on microgrid small-signal stability.

4) CURRENTS INJECTED BY VSGs IN THE MICROGRID

The d-axis currents injected by VSG 1, 2, and 3 in Fig.13a while applying the proposed control method at t = 5 s are 4.55 A, 4.67 A, 5.27 A, respectively. On the other hand, using the optimization method in [24] the d-axis currents injected by VSGs 1, 2, and 3 are 4.04 A, 4.49 A, and 5.91 A. Therefore the maximum d-axis current mismatch has been decreased from 1.87 A to 0.72 A by the proposed control method. As it is seen in Fig. 13b, the q-axis current overshoot while applying

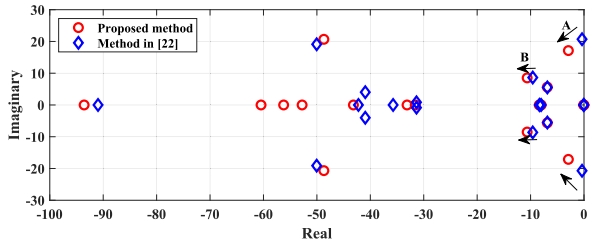

FIGURE 12. The dominant eigenvalues of microgrid applying the proposed optimal parameters and optimal parameters in [24].

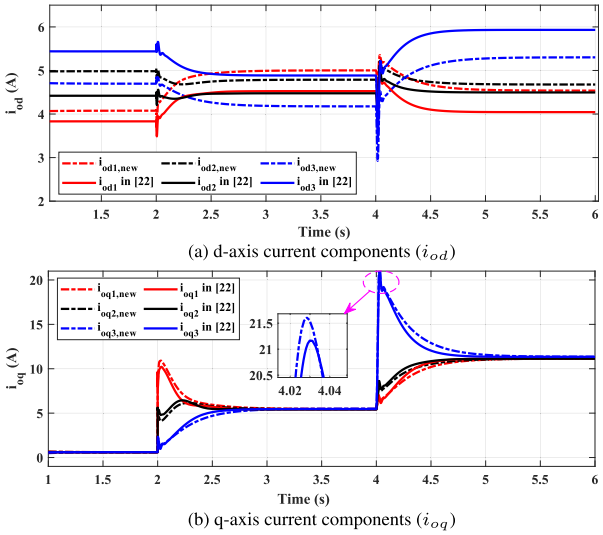

FIGURE 13. The microgrid current components while applying optimal parameters drawn by the proposed optimization algorithm and the optimization method in [24].

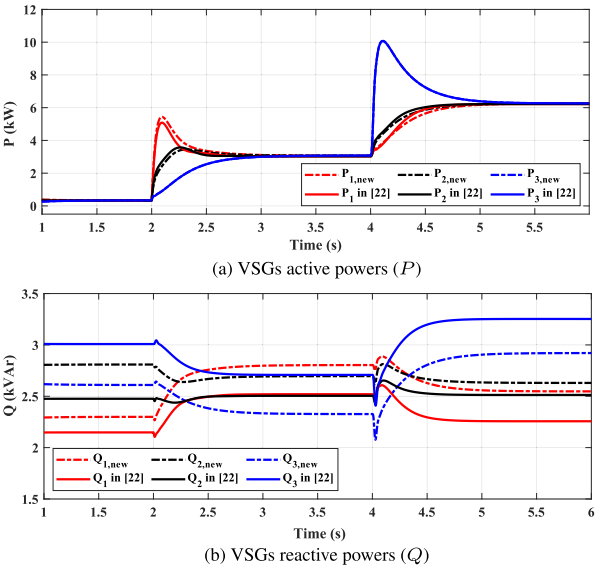

FIGURE 14. The active and reactive powers for VSGs 1, 2, 3 in load change scenario while applying the proposed optimal parameters and the optimal parameters in [24].

TABLE 5. Comparison of control methods.

Index	Proposed "VSG + VI + F" method	Method in [24]
Bus voltages control	Excellent	Good
Microgrid frequency control	Excellent	Good
Microgrid small-signal stability	Excellent	Poor
VSG current control	Excellent	Good
VSG current overshoot	Medium	Good
Active power sharing	Excellent	Excellent
Reactive power sharing	Excellent	Poor

the proposed control method in this study is a little greater than the current overshoot while applying the method in [24] (21.55 A and 21.16 A, respectively).

5) THE ACTIVE AND REACTIVE POWERS OF VSGs

The active powers supplied by VSGs in two cases in Fig.14a present a similar performance either by the proposed optimal parameters or by those optimal parameters drawn from [24]. After the load-change at t = 2 s any VSG injects 3.09 kW and after t = 4 s injects 6.22 kW.

The VSGs reactive powers at t = 5 s while applying the proposed optimal parameters in Fig. 14b are 2.54 kVAr, 2.62 kVAr and 2.91 kVAr for VSGs 1-3, respectively. On the other hand, while the optimal parameters drawn from [24] are applied, the VSGs inject 2.25 kVAr, 2.51 kVAr, 3.25 kVAr at t = 5 s, respectively. Consequently, the reactive power mismatches have been 0.37 kVAr and 1 kVAr while applying the proposed optimal parameters and the optimal parameters in [24]. Thereupon, the reactive power mismatches has been declined from 1 kVAR to 0.37 kVAR by the proposed optimization method.

Herein, in order to summarize and compare the simulation results drawn by the proposed "VSG + VI + F" optimization algorithm and the method in [24], the performance characteristics of these methods are compared in Table.5. For any index, the level of performance while using any method is declared. Obviously, the excellent is representative of an enhanced performance and the poor refers to unfavorable performance.

VI. CONCLUSION

The current research proposes a detailed modeling for a VSG-based islanded microgrid which is supplying different types of loads including static and dynamic loads. The effect of dynamic load on its corresponding bus and the other VSGs in microgrid are examined and corresponding permissible intervals for virtual impedances, virtual inertia, virtual damping and current state-feedback factor are drawn. The presence of a SIM is limiting the permissible virtual impedances to roughly one third of it for a VSG connected to the same bus. The low power SIM effect on the virtual inertia and damping is similar to the static load. The other prominent result is that the proposed optimization algorithm and objective function could optimally minimize the reactive power mismatches, enhance the microgrid small-signal stability, enhance the frequency nadir and decrease the voltage drops in buses in comparison to another recent research.

The microgrid model could include energy storage systems as another vital element. Moreover, the virtual intelligence methods can be applied to monitor the microgrid state and accomplish the parameters optimization online during the operation of microgrid. These two points highlight the prospective future research.

APPENDIX A
SIM MATRICES

The following matrices are used in section II for SIM dynamic modeling and in section III for small-signal stability analysis. The utilized parameters can be found in Table 2.

$$E = \frac{1}{\omega_b}\begin{pmatrix} X_{ss} & 0 & X_M & 0 & 0 \\ 0 & X_{ss} & 0 & X_M & 0 \\ X_M & 0 & X'_{rr} & 0 & 0 \\ 0 & X_M & 0 & X'_{rr} & 0 \\ 0 & 0 & 0 & 0 & -2H\omega_b \end{pmatrix} \tag{57}$$

$$F = -\begin{pmatrix} r_s & \frac{\omega_e}{\omega_b}X_{ss} & 0 & \frac{\omega_e}{\omega_b}X_M & 0 \\ -\frac{\omega_e}{\omega_b}X_{ss} & r_s & -\frac{\omega}{\omega_b}X_M & 0 & 0 \\ 0 & s_0\frac{\omega_e}{\omega_b}X_M & r'_r & s_0\frac{\omega_e}{\omega_b}X'_{rr} & 0 \\ -s_0\frac{\omega_e}{\omega_b}X_M & 0 & -s_0\frac{\omega_e}{\omega_b}X'_{rr} & 0 & 0 \\ X_M i'_{Dr0} & -X_M i'_{Qr0} & -X_M i_{Ds0} & 0 & 0 \\ 0 & 0 & 0 & 0 & 0 \\ 0 & 0 & 0 & 0 & 0 \\ s_0\frac{\omega_e}{\omega_b}X'_{rr} & -X_M i_{Ds0} - X'_{rr} i'_{Dr0} & 0 & 0 & 0 \\ r'_r & X_M . i_{Qs0} + X'_{rr} i'_{Qr0} & 0 & 0 & 0 \\ X_M i_{Qs0} & 0 & 0 & 0 & 0 \end{pmatrix} \tag{58}$$

APPENDIX B
MICROGRID SMALL-SIGNAL STABILITY MATRICES

The following matrices are applied in section III. It should be noted that the $I_{od,i}$, $I_{oq,i}$, $I_{ld,i}$, $I_{lq,i}$, $V_{od,i}$, and $V_{oq,i}$ are the dq components of output current, terminal current, and terminal voltage of VSG_i in the corresponding operating point.

$$A_2 = \begin{bmatrix} \overbrace{\cdots}^{zeros} & -k_{i,PLL} & k_{p,PLL} & 0 & 0 & 0 & 0 & 0 \\ \ddots & 0 & 0 & 0 & 0 & 0 & 0 & 0 \\ \cdots & 0 & 0 & 0 & 0 & 0 & 0 & 0 \end{bmatrix}_{12\times 16} \tag{59}$$

$$A_3 = \begin{bmatrix} 0 & & & & 0 & 0 & 0 & 0 & 0 \\ 0 & & & & 0 & 0 & 0 & 0 & 0 \\ \frac{V_{bD,i}.sin(\delta^0_{PLL,i}) - V_{bQ,i}.cos(\delta^0_{PLL,i})}{L_c} & & & & 0 & 0 & 0 & 0 & 0 \\ \frac{V_{bD,i}.cos(\delta^0_{PLL,i}) + V_{bQ,i}.sin(\delta^0_{PLL,i})}{L_c} & & & & 0 & 0 & 0 & 0 & 0 \\ 0 & \frac{1}{C_f} & 0 & k_{i,PLL}.V_{oq,i} & -k_{p,PLL}.V_{oq,i} & 0 \\ 0 & 0 & \frac{1}{C_f} & -k_{i,PLL}.V_{od,i} & k_{p,PLL}.V_{od,i} & 0 \\ 0 & 0 & 0 & 0 & 0 & 0 \\ 0 & 0 & 0 & 0 & 0 & 0 \end{bmatrix} \tag{60}$$

$$A_4 = \begin{bmatrix} 0 & \overbrace{\cdots}^{zeros} & 0 & k_{i,PLL}.V_{oq,i} \\ 0 & \overbrace{\cdots}^{zeros} & 0 & -k_{i,PLL}.V_{od,i} \\ 0 & \overbrace{\cdots}^{zeros} & 0 & k_{i,PLL}.I_{oq,i} \\ 0 & \overbrace{\cdots}^{zeros} & 0 & -k_{i,PLL}.I_{od,i} \end{bmatrix}$$
$$\begin{bmatrix} -k_{p,PLL}.V_{oq,i} & 0 & 0 & 0 & 0 & 0 \\ k_{p,PLL}.V_{od,i} & 0 & 0 & 0 & 0 & 0 \\ -k_{p,PLL}.I_{oq,i} & 0 & 0 & 0 & 0 & 0 \\ k_{p,PLL}.I_{od,i} & 0 & 0 & 0 & 0 & 0 \end{bmatrix}_{4\times 16} \tag{61}$$

$$A_5 = \begin{bmatrix} 0 & 0 \\ 0 & 0 \\ \frac{r_N}{L_c}.cos(\delta^0_{PLL,i}) & \frac{r_N}{L_c}.sin(\delta^0_{PLL,i}) \\ -\frac{r_N}{L_c}.sin(\delta^0_{PLL,i}) & \frac{r_N}{L_c}.cos(\delta^0_{PLL,i}) \end{bmatrix}_{4\times 2} \tag{62}$$

$$A_6 = \begin{bmatrix} 0 & 0 & 0 & 0 & 0 \\ 0 & 0 & & & \\ \frac{r_N}{L_c}.sin(\delta^0_{PLL,i}) & \frac{r_N}{L_c}.cos(\delta^0_{PLL,i}) & 0 & 0 & 0 \\ \frac{r_N}{L_c}.cos(\delta^0_{PLL,i}) & -\frac{r_N}{L_c}.sin(\delta^0_{PLL,i}) & 0 & 0 & 0 \\ 0 & 0 & 0 & 0 & 0 \end{bmatrix}_{4\times 5} \tag{63}$$

$$A_7 = \begin{bmatrix} 0 & 0 \\ 0 & 0 \\ -\frac{r_N}{L_c}.cos(\delta^0_{PLL,i}) & -\frac{r_N}{L_c}.sin(\delta^0_{PLL,i}) \\ \frac{r_N}{L_c}.sin(\delta^0_{PLL,i}) & -\frac{r_N}{L_c}.cos(\delta^0_{PLL,i}) \end{bmatrix}_{4\times 2} \tag{64}$$

$$A_{10} = \begin{bmatrix} -\frac{r_N}{L_{line,ij}} & 0 \\ 0 & -\frac{r_N}{L_{line,ij}} \end{bmatrix}_{2\times 2} \tag{65}$$

$$A_{11} = \begin{bmatrix} 0 & -\frac{r_N}{L_{line,ij}} & 0 & 0 & 0 \\ -\frac{r_N}{L_{line,ij}} & 0 & 0 & 0 & 0 \end{bmatrix}_{2\times 5} \tag{66}$$

$$A_8 = \begin{bmatrix} -(\frac{r_N}{L_{line,ij}}).(sin(\delta^0_{PLL,i}).I_{od,i} + cos(\delta^0_{PLL,i}).I_{oq,i}) \\ (\frac{r_N}{L_{line,ij}}).(cos(\delta^0_{PLL,i}).I_{od,i} - sin(\delta^0_{PLL,i}).I_{oq,i}) \end{bmatrix}$$
$$\begin{bmatrix} 0 & \overbrace{\cdots}^{zeros} & k_{i,PLL}.I_{line,ijQ} & -k_{p,PLL}.I_{line,ijQ} & 0 & 0 & 0 \\ 0 & \overbrace{\cdots}^{zeros} & -k_{i,PLL}.I_{line,ijD} & k_{p,PLL}.I_{line,ijD} & 0 & 0 & 0 \\ (\frac{r_N}{L_{line,ij}}).cos(\delta^0_{PLL,i}) & & -(\frac{r_N}{L_{line,ij}}).sin(\delta^0_{PLL,i}) & & & & \\ (\frac{r_N}{L_{line,ij}}).sin(\delta^0_{PLL,i}) & & (\frac{r_N}{L_{line,ij}}).cos(\delta^0_{PLL,i}) & & & & \end{bmatrix}_{2\times 16} \tag{68}$$

$$A_9 = \begin{bmatrix} (\frac{r_N}{L_{line,ij}}).(sin(\delta^0_{PLL,j}).I_{od,j} + cos(\delta^0_{PLL,j}).I_{oq,j}) \\ -(\frac{r_N}{L_{line,ij}}).(cos(\delta^0_{PLL,j}).I_{od,j} - sin(\delta^0_{PLL,j}).I_{oq,j}) \end{bmatrix}$$
$$\begin{matrix} 0 & 0 & 0 & 0 & 0 & 0 & 0 & 0 & 0 & 0 & 0 & 0 & 0 & 0 \\ 0 & 0 & 0 & 0 & 0 & 0 & 0 & 0 & 0 & 0 & 0 & 0 & 0 & 0 \end{matrix}$$

$$A_1 = \begin{bmatrix} 0 & 0 & 0 & 0 & 0 & 0 & 0 & 0 & 0 & k_{i,PLL} \\ 0 & -\omega_c & 0 & 0 & 0 & 0 & 0 & 0 & 0 & 0 \\ 0 & 0 & -\omega_c & 0 & 0 & 0 & 0 & 0 & 0 & 0 \\ 0 & 0 & 0 & 0 & 0 & 0 & 0 & 0 & 0 & k_{i,PLL} \\ 0 & 0 & -n_q & 0 & 0 & 0 & 0 & 0 & 0 & 0 \\ 0 & 0 & 0 & k_{iv} & 0 & 0 & 0 & -1 & 0 & k_{pv}.k_{p,PLL} \\ 0 & 0 & -k_{pv}.n_q & 0 & k_{iv} & 0 & 0 & 0 & -1 & 0 \\ 0 & 0 & 0 & \frac{k_{pc}.k_{iv}}{L_f} & 0 & \frac{k_{ic}}{L_f} & 0 & -\frac{r_f}{L_f}-\frac{k_{pc}}{L_f} & \omega_{PLL,i}-\omega_n & \frac{k_{pc}.k_{pv}.k_{i,PLL}}{L_f}+I_{lq,i}.k_{i,PLL} \\ 0 & 0 & \frac{-k_{pc}.k_{pv}.n_q}{L_f} & 0 & \frac{k_{pc}.k_{iv}}{L_f} & 0 & \frac{k_{ic}}{L_f} & \omega_n-\omega_{PLL,i} & \frac{-r_f-k_{pc}}{L_f} & -k_{i,PLL}.I_{ld,i} \\ 0 & 0 & 0 & 0 & 0 & 0 & 0 & 0 & 0 & 0 \\ 0 & 0 & 0 & 0 & 0 & 0 & 0 & 0 & 0 & 0 \\ 0 & \frac{-1}{\omega_n.J_i} & 0 & 0 & 0 & 0 & 0 & 0 & 0 & -\frac{K_f.k_{i,PLL}}{J_i} \end{bmatrix}$$

$$\begin{bmatrix} -k_{p,PLL} & 0 & 0 & 0 & 0 & 0 \\ 0 & 0 & 1.5.\omega_c.I_{od,i} & 1.5.\omega_c.I_{oq,i} & 1.5.\omega_c.V_{od,i} & 1.5.\omega_c.V_{oq,i} \\ 0 & 0 & -1.5.\omega_c.I_{oq,i} & 1.5.\omega_c.I_{od,i} & 1.5.\omega_c.V_{oq,i} & -1.5.\omega_c.V_{od,i} \\ -k_{p,PLL} & -1 & 0 & 0 & 0 & 0 \\ 0 & 0 & 0 & -1 & -X_{v,i} & -R_{v,i} \\ -k_{pv}.k_{p,PLL} & -k_{pv} & 0 & 0 & F & 0 \\ 0 & 0 & 0 & -k_{pv} & -X_{v,i}.k_{pv} & F-R_{v,i}.k_{pv} \\ -\frac{k_{pc}.k_{pv}.k_{p,PLL}}{L_f}-I_{lq,i}.k_{i,PLL} & \frac{-k_{pc}.k_{pv}}{L_f} & \frac{-1}{L_f} & 0 & \frac{F.k_{pc}}{L_f} & 0 \\ k_{p,PLL}.I_{ld,i} & 0 & 0 & \frac{-k_{pc}.k_{pv}-1}{L_f} & \frac{-X_{v,i}.k_{pc}.k_{pv}}{L_f} & \frac{-R_{v,i}.k_{pc}.k_{pv}}{L_f}+\frac{F.k_{pc}}{L_f} \\ -1 & 0 & 0 & 0 & 0 & 0 \\ -\omega_{c,PLL} & 0 & \omega_{c,PLL} & 0 & 0 & 0 \\ \frac{K_f.k_{p,PLL}}{J_i} & \frac{-D_i}{J_i} & 0 & 0 & 0 & 0 \end{bmatrix}_{12\times 16} \quad (67)$$

$$A_{13} = \begin{bmatrix} -(\frac{r_N}{L_{load,i}}).(sin(\delta^0_{PLL,i}).I_{od,i}+cos(\delta^0_{PLL,i}).I_{oq,i}) & \overbrace{\cdots}^{zeros} & (\frac{r_N}{L_{load,i}}).cos(\delta^0_{PLL,i}) & -(\frac{r_N}{L_{load,i}}).sin(\delta^0_{PLL,i}) \\ (\frac{r_N}{L_{load,i}}).(cos(\delta^0_{PLL,i}).I_{od,i}-sin(\delta^0_{PLL,i}).I_{oq,i}) & \overbrace{\cdots}^{zeros} & (\frac{r_N}{L_{load,i}}).sin(\delta^0_{PLL,i}) & (\frac{r_N}{L_{load,i}}).cos(\delta^0_{PLL,i}) \end{bmatrix}_{2\times 16} \quad (76)$$

$$A_{19} = \begin{bmatrix} r_N.(cos(\delta^0_{PLL,i}).I_{od,i}-sin(\delta^0_{PLL,i}).I_{oq,i}) & \overbrace{\cdots}^{zeros} & r_N.sin(\delta^0_{PLL,i}) & r_N.cos(\delta^0_{PLL,i}) \\ r_N.(-sin(\delta^0_{PLL,i}).I_{od,i}-cos(\delta^0_{PLL,i}).I_{oq,i}) & \overbrace{\cdots}^{zeros} & r_N.cos(\delta^0_{PLL,i}) & -r_N.sin(\delta^0_{PLL,i}) \\ 0 & \overbrace{\cdots}^{zeros} & 0 & 0 \\ 0 & \overbrace{\cdots}^{zeros} & 0 & 0 \\ 0 & \overbrace{\cdots}^{zeros} & 0 & 0 \end{bmatrix}_{5\times 16} \quad (77)$$

$$\begin{bmatrix} -(\frac{r_N}{L_{line,ij}}).cos(\delta^0_{PLL,j}) & (\frac{r_N}{L_{line,ij}}).sin(\delta^0_{PLL,j}) \\ -(\frac{r_N}{L_{line,ij}}).sin(\delta^0_{PLL,j}) & -(\frac{r_N}{L_{line,ij}}).cos(\delta^0_{PLL,j}) \end{bmatrix}_{2\times 16} \quad (69)$$

$$A_{12} = \begin{bmatrix} \frac{-r_{line,ij}-r_N-r_N}{L_{line,ij}} & \omega^0_{PLL,j} \\ -\omega^0_{PLL,j} & \frac{-r_{line,ij}-r_N-r_N}{L_{line,ij}} \end{bmatrix}_{2\times 2} \quad (70)$$

$$A_{14} = \begin{bmatrix} 0 \overbrace{\cdots}^{zeros} & k_{i,PLL}.I_{loadQ,i} & -k_{p,PLL}.I_{loadQ,i} \\ 0 \overbrace{\cdots}^{zeros} & -k_{i,PLL}.I_{loadD,i} & k_{p,PLL}.I_{loadD,i} \end{bmatrix}$$

$$\begin{bmatrix} 0 & 0 & 0 & 0 & 0 \\ 0 & 0 & 0 & 0 & 0 \end{bmatrix}_{2\times 16} \quad (71)$$

$$A_{15} = \begin{bmatrix} \frac{-r_{load,i}-r_N}{L_{load,i}} & \omega^0_{PLL,i} \\ -\omega^0_{PLL,i} & \frac{-r_{load,i}-r_N}{L_{load,i}} \end{bmatrix}_{2\times 2} \quad (72)$$

$$A_{16} = \begin{bmatrix} 0 & -\frac{r_N}{L_{load,i}} & 0 & 0 & 0 \\ -\frac{r_N}{L_{load,i}} & 0 & 0 & 0 & 0 \end{bmatrix}_{2\times 5} \quad (73)$$

$$A_{17} = \begin{bmatrix} -\frac{r_N}{L_{load,i}} & 0 \\ 0 & -\frac{r_N}{L_{load,i}} \end{bmatrix}_{2\times 2} \quad (74)$$

$$A_{18} = \begin{bmatrix} -r_N & 0 & 0 & 0 & 0 \\ 0 & -r_N & 0 & 0 & 0 \\ 0 & 0 & 0 & 0 & 0 \\ 0 & 0 & 0 & 0 & 0 \\ 0 & 0 & 0 & 0 & 0 \end{bmatrix}_{5\times5} \tag{75}$$

$$A_{20} = \begin{bmatrix} r_N & 0 \\ 0 & r_N \\ 0 & 0 \\ 0 & 0 \\ 0 & 0 \end{bmatrix}_{5\times2} \tag{78}$$

$$A_{21} = \begin{bmatrix} 0 & r_N \\ r_N & 0 \\ 0 & 0 \\ 0 & 0 \\ 0 & 0 \end{bmatrix}_{5\times2} \tag{79}$$

REFERENCES

[1] M. Farrokhabadi *et al.*, "Microgrid stability definitions, analysis, and examples," *IEEE Trans. Power Syst.*, vol. 35, no. 1, pp. 13–29, Jan. 2020.
[2] N. Pogaku, M. Prodanovic, and T. C. Green, "Modeling, analysis and testing of autonomous operation of an inverter-based microgrid," *IEEE Trans. Power Electron.*, vol. 22, no. 2, pp. 613–625, Mar. 2007.
[3] U. Tamrakar, D. Shrestha, M. Maharjan, B. P. Bhattarai, T. M. Hansen, and R. Tonkoski, "Virtual inertia: Current trends and future directions," *Appl. Sci.*, vol. 7, no. 7, p. 654, Jun. 2017.
[4] A. Karimi, Y. Khayat, M. Naderi, T. Dragicevic, R. Mirzaei, F. Blaabjerg, and H. Bevrani, "Inertia response improvement in AC microgrids: A fuzzy-based virtual synchronous generator control," *IEEE Trans. Power Electron.*, vol. 35, no. 4, pp. 4321–4331, Apr. 2020.
[5] M. Li, W. Huang, N. Tai, L. Yang, D. Duan, and Z. Ma, "A dual-adaptivity inertia control strategy for virtual synchronous generator," *IEEE Trans. Power Syst.*, vol. 35, no. 1, pp. 594–604, Jan. 2020.
[6] M. Li, Y. Wang, Y. Liu, N. Xu, S. Shu, and W. Lei, "Enhanced power decoupling strategy for virtual synchronous generator," *IEEE Access*, vol. 8, pp. 73601–73613, 2020.
[7] W. Zhang, X. Yan, and H. Huang, "Performance tuning for power electronic interfaces under VSG control," *Appl. Sci.*, vol. 10, no. 3, p. 953, Feb. 2020.
[8] J. Liu, Y. Miura, and T. Ise, "Fixed-parameter damping methods of virtual synchronous generator control using state feedback," *IEEE Access*, vol. 7, pp. 99177–99190, 2019.
[9] Y. Yan, D. Shi, D. Bian, B. Huang, Z. Yi, and Z. Wang, "Small-signal stability analysis and performance evaluation of microgrids under distributed control," *IEEE Trans. Smart Grid*, vol. 10, no. 5, pp. 4848–4858, Sep. 2019.
[10] H. Wu, X. Ruan, D. Yang, X. Chen, W. Zhao, Z. Lv, and Q.-C. Zhong, "Small-signal modeling and parameters design for virtual synchronous generators," *IEEE Trans. Ind. Electron.*, vol. 63, no. 7, pp. 4292–4303, Jul. 2016.
[11] S. Leitner, M. Yazdanian, A. Mehrizi-Sani, and A. Muetze, "Small-signal stability analysis of an inverter-based microgrid with internal model-based controllers," *IEEE Trans. Smart Grid*, vol. 9, no. 5, pp. 5393–5402, Sep. 2018.
[12] V. N. Kumar and S. K. Parida, "Parameter optimization of universal droop and internal model controller for multi inverter-fed DGs based on accurate small-signal model," *IEEE Access*, vol. 7, pp. 101928–101940, 2019.
[13] Y. Pan, L. Chen, X. Lu, J. Wang, F. Liu, and S. Mei, "Stability region of droop-controlled distributed generation in autonomous microgrids," *IEEE Trans. Smart Grid*, vol. 10, no. 2, pp. 2288–2300, Mar. 2019.
[14] M. A. Mahmud, H. R. Pota, M. Aldeen, and M. J. Hossain, "Partial feedback linearizing excitation controller for multimachine power systems to improve transient stability," *IEEE Trans. Power Syst.*, vol. 29, no. 2, pp. 561–571, Mar. 2014.
[15] A. Firdaus and S. Mishra, "Mitigation of power and frequency instability to improve load sharing among distributed inverters in microgrid systems," *IEEE Syst. J.*, vol. 14, no. 1, pp. 1024–1033, Mar. 2020.
[16] J. Chen and J. Chen, "Stability analysis and parameters optimization of islanded microgrid with both ideal and dynamic constant power loads," *IEEE Trans. Ind. Electron.*, vol. 65, no. 4, pp. 3263–3274, Apr. 2018.
[17] B. Pournazarian, M. Saeedian, B. Eskandari, M. Lehtonen, and E. Pouresmaeil, "Feasible ranges of microgrid parameters based on small-signal stability analysis," in *Proc. IEEE 21st Workshop Control Modeling Power Electron. (COMPEL)*, Nov. 2020, pp. 1–6.
[18] M. Rasheduzzaman, J. A. Mueller, and J. W. Kimball, "An accurate small-signal model of inverter-dominated islanded microgrids using *dq* reference frame," *IEEE J. Emerg. Sel. Topics Power Electron.*, vol. 2, no. 4, pp. 1070–1080, Dec. 2014.
[19] A. Kahrobaeian and Y. A.-R. I. Mohamed, "Analysis and mitigation of low-frequency instabilities in autonomous medium-voltage converter-based microgrids with dynamic loads," *IEEE Trans. Ind. Electron.*, vol. 61, no. 4, pp. 1643–1658, Apr. 2014.
[20] S. Mortazavian and Y. A.-R.-I. Mohamed, "Investigation and enhancement of stability in grid-connected converter-based distributed generation units with dynamic loads," *IEEE Access*, vol. 8, pp. 93426–93443, 2020.
[21] L. Zhang, S. Ji, S. Gu, X. Huang, J. E. Palmer, W. Giewont, F. F. Wang, and L. M. Tolbert, "Design considerations for high-voltage insulated gate drive power supply for 10-kV SiC MOSFET applied in medium-voltage converter," *IEEE Trans. Ind. Electron.*, vol. 68, no. 7, pp. 5712–5724, Jul. 2021.
[22] T. Wen, X. Zou, D. Zhu, X. Guo, L. Peng, and Y. Kang, "Comprehensive perspective on virtual inductor for improved power decoupling of virtual synchronous generator control," *IET Renew. Power Gener.*, vol. 14, no. 4, pp. 485–494, Mar. 2020.
[23] X. Wu, C. Shen, and R. Iravani, "Feasible range and optimal value of the virtual impedance for droop-based control of microgrids," *IEEE Trans. Smart Grid*, vol. 8, no. 3, pp. 1242–1251, May 2017.
[24] B. Pournazarian, S. S. Seyedalipour, M. Lehtonen, S. Taheri, and E. Pouresmaeil, "Virtual impedances optimization to enhance microgrid small-signal stability and reactive power sharing," *IEEE Access*, vol. 8, pp. 139691–139705, 2020.
[25] M. A. Mahmud, M. J. Hossain, H. R. Pota, and A. M. T. Oo, "Robust nonlinear distributed controller design for active and reactive power sharing in islanded microgrids," *IEEE Trans. Energy Convers.*, vol. 29, no. 4, pp. 893–903, Dec. 2014.
[26] B. K. Unnikrishnan, M. S. Johnson, and E. P. Cheriyan, "Small signal stability improvement of a microgrid by the optimised dynamic droop control method," *IET Renew. Power Gener.*, vol. 14, no. 5, pp. 822–833, Apr. 2020.
[27] L. Zhang and X. Ruan, "Control schemes for reducing second harmonic current in two-stage single-phase converter: An overview from DC-bus port-impedance characteristics," *IEEE Trans. Power Electron.*, vol. 34, no. 10, pp. 10341–10358, Oct. 2019.
[28] J. He, X. Wu, X. Wu, Y. Xu, and J. M. Guerrero, "Small-signal stability analysis and optimal parameters design of microgrid clusters," *IEEE Access*, vol. 7, pp. 36896–36909, 2019.
[29] X. Wu and C. Shen, "Distributed optimal control for stability enhancement of microgrids with multiple distributed generators," *IEEE Trans. Power Syst.*, vol. 32, no. 5, pp. 4045–4059, Sep. 2017.
[30] Y. Li, Z. Shuai, X. Liu, Y. Hong, X. Wu, and Z. J. Shen, "Stability investigation of bidirectional AC-DC converter considering operating conditions," *IEEE Access*, vol. 8, pp. 131499–131510, 2020.
[31] P. Krause, O. Wasynczuk, S. D. Sudhoff, and S. D. Pekarek, *Analysis of Electric Machinery and Drive Systems*, 3rd ed. Hoboken, NJ, USA: Wiley, 2013.
[32] H. Zhao, Q. Yang, and H. Zeng, "Multi-loop virtual synchronous generator control of inverter-based DGs under microgrid dynamics," *IET Gener., Transmiss. Distrib.*, vol. 11, no. 3, pp. 795–803, Feb. 2017.
[33] M. R. AlRashidi and M. E. El-Hawary, "A survey of particle swarm optimization applications in electric power systems," *IEEE Trans. Evol. Comput.*, vol. 13, no. 4, pp. 913–918, Aug. 2009.

BAHRAM POURNAZARIAN (Graduate Student Member, IEEE) received the B.Sc. degree in electrical power engineering from Razi University, Kermanshah, Iran, in 2012, and the M.Sc. degree in electrical power engineering from Amirkabir University of Technology (Tehran Polytechnic), Tehran, Iran, in 2016. He is currently pursuing the Ph.D. degree in power electronics engineering with Aalto University, Espoo, Finland. His research interests include microgrids modeling, control and stability, grid integration of renewable energy sources, and heuristic optimization algorithms.

REZA SANGRODY received the B.Sc. and M.Sc. degrees in electrical engineering from Mazandaran University, in 2003 and 2005, respectively.

Since 2005, he has been a Lecturer with Islamic Azad University Firoozkooh Branch. Since 2012, he has been working as a Consultant Engineer with Behjosh Electric Factory for designing and producing different types of welding machines. He has published more than 20 journal and conference papers in the field of power electronics applications. His current research interests include power electronic circuit design and control, application of power electronic converters in smart grids, photovoltaic and wind energy harvesting, and electrical machines drivers design and control.

MEYSAM SAEEDIAN was born in 1991. He received the B.Sc. degree in electrical engineering from Arak University of Technology, Arak, Iran, in 2014, and the M.Sc. degree from Babol Noshirvani University of Technology, Babol, Iran, in 2017. He is currently pursuing the Ph.D. degree with the Department of Electrical Engineering and Automation, Aalto University, Espoo, Finland. His research interests include the design of power electronic converters, control systems, grid voltage and frequency stability, and RES integration.

MATTI LEHTONEN received the master's and Licentiate degrees in electrical engineering from Helsinki University of Technology, in 1984 and 1989, respectively, and the Doctor of Technology degree from Tampere University of Technology, in 1992. He was with VTT Energy, Espoo, Finland, from 1987 to 2003. Since 1999, he has been a Professor with Helsinki University of Technology. He is currently with Aalto University, where he is the Head of Power Systems and High Voltage Engineering. His main activities include power system planning and asset management, power system protection including earth fault problems, harmonics-related issues, and applications of information technology in distribution systems.

EDRIS POURESMAEIL (Senior Member, IEEE) received the Ph.D. degree in electrical engineering from the Technical University of Catalonia (UPC-Barcelona Tech), Barcelona, Spain, in 2012. After his Ph.D. degree, he joined the University of Waterloo, Waterloo, Canada, as a Postdoctoral Research Fellow and then joined the University of Southern Denmark (SDU), Odense, Denmark, as an Associate Professor. He is currently an Associate Professor with the Department of Electrical Engineering and Automation (EEA), Aalto University, Espoo, Finland. His main research activities focus on the application of power electronics in power and energy sectors.